

PROCEEDINGS OF SPIE

SPIDigitalLibrary.org/conference-proceedings-of-spie

Reproducibility of two calibration procedures for phase-measuring deflectometry

Allgeier, Stephan, Gengenbach, Ulrich, Köhler, Bernd, Reichert, Klaus-Martin, Hagenmeyer, Veit

Stephan Allgeier, Ulrich Gengenbach, Bernd Köhler, Klaus-Martin Reichert, Veit Hagenmeyer, "Reproducibility of two calibration procedures for phase-measuring deflectometry," Proc. SPIE 11490, Interferometry XX, 114900G (21 August 2020); doi: 10.1117/12.2567092

SPIE.

Event: SPIE Optical Engineering + Applications, 2020, Online Only

Reproducibility of two calibration procedures for phase-measuring deflectometry

Stephan Allgeier, Ulrich Gengenbach, Bernd Köhler, Klaus-Martin Reichert, and Veit Hagenmeyer

Institute for Automation and Applied Informatics, Karlsruhe Institute of Technology (KIT),
Hermann-von-Helmholtz-Platz 1, 76344 Eggenstein-Leopoldshafen, Germany

ABSTRACT

Phase-measuring deflectometry is an optical inspection technique for reflective surfaces. It enables absolute, quantitative surface measurements, given a calibrated measurement setup. Two general calibration approaches can be found in literature: First, the stepwise approach uses a calibration pattern and determines internal camera parameters and external geometrical parameters in separate, consecutive steps. Second, the holistic approach optimizes all parameters collectively, based on deflectometric measurements of a calibration mirror.

Whereas both approaches have been compared regarding the accuracy of subsequent surface measurements, the present contribution focuses on experimental examination of their reproducibility. In experiment E1, we assess the parameter variability by repeating both calibration procedures ten times. In an additional experiment E2, we repeat all calibration measurements related to a mirror/pattern position ten times in a row before rearranging the mirror/pattern, in order to examine the purely noise-related parameter variability. Finally, we calculate the coordinate variability of a set of world points projected onto the image planes of the calibrated cameras.

The measured variability is consistently higher in E1 than in E2 (average ratio: 3.2). Unexpectedly, in both experiments, the external parameter variability also turns out to be higher for the holistic approach compared to stepwise calibration (average ratio: 2.3). This is of importance, since the holistic approach is known from literature to be more accurate than the stepwise approach, regarding their respective application to surface measurements. The image coordinate variability is comparable for both calibration approaches with an average of 0.84 and 0.21 camera pixels for E1 and E2, respectively.

Keywords: printed electronics, surface inspection, deflectometry, calibration, reproducibility

1. INTRODUCTION

Functional printing, e.g. ink-jet printing, is a promising technology to fabricate smart, low-cost electronic devices and systems on flexible foil substrates such as wearables, Internet of Things (IoT) devices and sensors.^{1–3} Besides the functional inks, frequently based on novel nanomaterials, another key component of printed electronics are the foil substrates. In many cases these foils are made of standard materials such as Polyethyleneterephthalate (PET) or Polyimide (PI), but nanomaterials are also applied to integrate functionality into the substrate.⁴ Substrate planarity is an important issue for achieving high quality printing results as the ink-jet printing process is sensitive to alterations of the distance between the substrate and the printing nozzle. Factors influencing foil substrate planarity are the foil fabrication process and post-processing procedures in between multiple printing steps. Due to roll-to-roll fabrication processes, foil substrates often exhibit internal strain-induced warpage around one of their main axes. Moreover post-processing steps such as oven sintering or Laser sintering of the printed structures may lead to local warpage. Hence, foil warpage detection and subsequent warpage management are key requirements for reliable, high precision functional printing processes.

Phase-measuring deflectometry (PMD) is a technique for optical inspection of reflective surfaces. The basic setup consists of one or more cameras, a pattern screen that can show predefined patterns, and the surface under

Corresponding author: Stephan Allgeier, stephan.allgeier@kit.edu

Interferometry XX, edited by Michael B. North Morris, Katherine Creath,
Rosario Porras-Aguilar, Proc. of SPIE Vol. 11490, 114900G · © 2020
SPIE · CCC code: 0277-786X/20/\$21 · doi: 10.1117/12.2567092

Proc. of SPIE Vol. 11490 114900G-1

test. The cameras are directed at the surface under test and acquire images of the reflected patterns on the screen. In PMD, the patterns are sine-modulated intensity functions. Their phase effectively encodes the screen coordinates.^{5,6} This allows the calculation of correspondence maps between camera pixels and screen coordinates; these correspondence maps are also called phase maps and are the basis for diverse analysis techniques to reveal information about the surface under test. PMD is extremely sensitive to local changes of the surface gradient⁵⁻⁷ and can be used for qualitative inspection purposes, such as defect detection, without the need for preceding calibration.⁵

Given a calibrated measurement setup, it is also applicable to absolute, quantitative surface measurement tasks, such as full-field surface reconstruction. Different calibration procedures have been proposed in the literature, most of which fall into one of two general categories. The stepwise approach⁸⁻¹¹ first determines internal parameters of the underlying camera model, generally using a calibration pattern, followed by the geometrical calibration of the screen-camera setup, i.e. the external parameters (depending on the setup, an additional step for internal screen calibration must sometimes be included^{8,9}). The holistic approach¹²⁻¹⁴ on the other hand is based on repeated deflectometric measurements of a planar calibration mirror in varying poses. All internal and external parameters are thereafter optimized collectively to fit to the taken measurements.

The evaluation of published calibration techniques is generally provided by performing deflectometric measurements with the calibrated setups using specimens of known shape, e.g. high-precision planar or spherical mirrors, and examining the deviation of the reconstructed surface from the ideal shape. A direct comparison of both calibration methods has reported a significantly better measurement accuracy for the holistic approach, reducing the global surface error by a factor of three to six compared with the stepwise approach.¹²

The objective of the present contribution is to complement these published observations with an experimental investigation of the reproducibility of both calibration approaches, i.e. the variability of the internal and external parameters obtained by repeating the calibration procedures under the same conditions. The setup used for the experiments is comparable to those reported by other research groups.^{5,6} A standard computer monitor is used to display the patterns. The setup includes three cameras capturing the measurement space in order to generally provide an extended range of surface gradients that can be measured, but also to enable the application of stereo- or multi-camera-based methods for surface reconstruction. The cameras are modeled as pinhole cameras with additional lens distortion correction terms.

Section 2 provides the mathematical model of the measurement setup used for calibration, including in particular all the model parameters that are calculated by the calibration techniques. Section 3 contains the descriptions of the stepwise and holistic calibration procedures, as implemented for the experiments. Section 4 describes in detail the conducted experiments and the variables measured for the assessment of the reproducibility of the calibration procedures. Section 5 provides a comprehensive presentation of the experimental results and Sec. 6 discusses and interprets the results, particularly with regard to how they relate to previously published comparative analyses.

2. MEASUREMENT MODEL

There is a large body of literature describing the deflectometric measurement process in detail.⁵⁻⁷ The general deflectometric measurement principle illustrated schematically in Fig. 1 applies to the majority of setups found in the published literature. It is used as the basis for the descriptions of the calibration processes and the experiments presented in Secs. 3 and 4. As the focus of the present contribution is on calibration, the following description of the deflectometric measurement process is kept short; its main purpose is to identify and introduce the relevant setup variables that have to be determined during calibration.

The deflectometric measurement process is based on the aforementioned correspondences between camera pixels and screen coordinates that are established by encoding the screen coordinates in the phase information of the special patterns used in PMD.^{6,8} Let $M(\vec{i}, \vec{x}_s)$ be such a correspondence map between camera image pixels $\vec{i} = (x_i, y_i)^T \in R^2$ and screen points $\vec{x}_s = (x_s, y_s, z_s)^T \in R^3$. The essential idea behind absolute, quantitative surface measurements then is to back-trace the light path from each \vec{i} to the screen position \vec{x}_s where it was emitted. Using the law of reflection, the surface normal vector \vec{n} is the bisection vector between \vec{v}_c and \vec{v}_s .

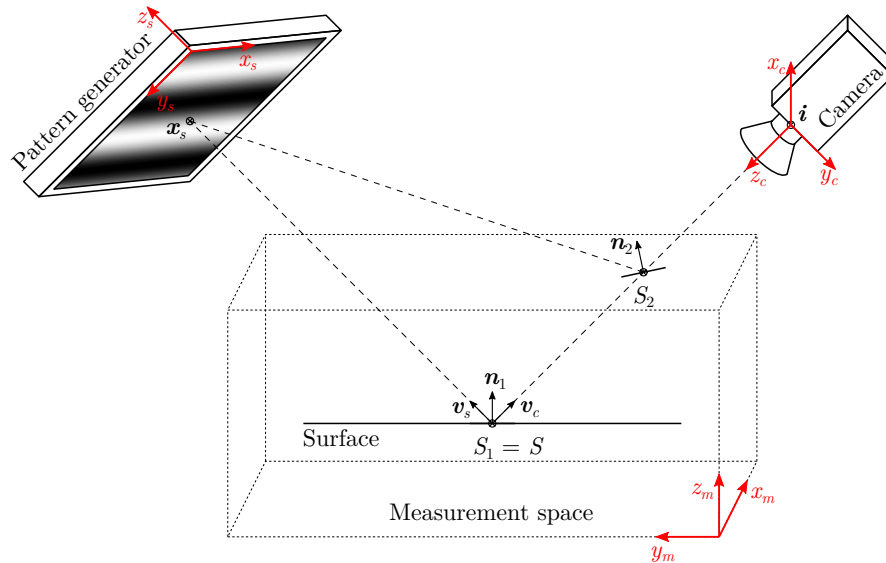


Figure 1. Schematic illustration of the deflectometric measurement process. Given the correspondence between camera pixel \vec{i} and screen point \vec{x}_s , S_i are potential surface points that are in agreement with the measurement. The potential surface normal vector \vec{n}_i at those points is the bisection vector between vectors \vec{v}_c and \vec{v}_s . The screen, camera and measurement coordinate systems, (x_s, y_s, z_s) , (x_c, y_c, z_c) and (x_m, y_m, z_m) , respectively, are shown in red.

Whereas the “view ray” \vec{v}_c is usually known (as described below) in absolute deflectometry measurements, the incident light ray \vec{v}_s is commonly unknown. As a consequence, each point S_i along \vec{v}_c is a potential surface point with a potential surface normal vector \vec{n}_i (see Fig. 1). Different solutions to this inherent ambiguity have been proposed, such as stereo-deflectometry,⁸ setups with two screens (or screen positions),^{15,16} supplementary measurements,¹⁷ or mathematical regularization.^{18–21}

The above short explanation of the measurement process implicitly assumes several pieces of a priori knowledge:

1. the geometric arrangement of the setup, i.e. the position and orientation of the screen and the camera,
2. the correspondence between pattern coordinates and screen coordinates, i.e. a (bijective) transformation function, and
3. the correspondence between camera image pixels and the respective view rays, i.e. a camera model that provides an (invertible) projection function.

The geometric arrangement of point 1 is described by a coordinate transformation matrix T_{sc} between the (both three-dimensional Cartesian) coordinate systems of the screen and the camera. W.l.o.g. we take the screen to define the reference coordinate system in which the camera position and orientation is described by six parameters: its three origin coordinates (the camera center) $\vec{o} = (o_x, o_y, o_z)^T$, and three rotation angles α , β and γ . Our specific implementation uses Givens rotations,²² but there are numerous other ways to describe an arbitrary 3D rotation by three parameters.^{22,23}

The experimental setup used throughout the present paper—as most of the commonly used setups—includes a computer monitor for pattern presentation. Assuming a regular grid of square pixels, pattern coordinates and screen coordinates are considered as interchangeable (i.e. an identity transformation function is assumed). A calibration is therefore not required for point 2. It should be noted that this applies to most, but not all proposed deflectometry setups. Notably, if the patterns are projected onto a (e.g. ground glass) screen, an explicit model for—and calibration of—the pattern-screen transformation function is required.⁸

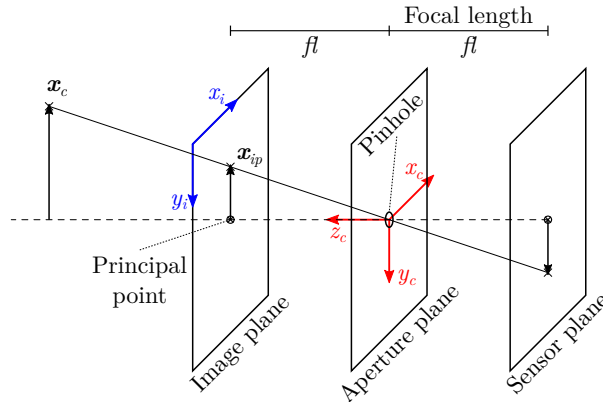


Figure 2. Schematic illustration of the pinhole camera model. A point \vec{x}_c in the field of view of the camera is projected onto the sensor plane through the pinhole in the aperture plane. A (virtual) image plane is arranged in front of the pinhole at the same distance as the sensor plane. All three planes are parallel. The projection \vec{x}_{ip} of \vec{x}_c onto the image plane is calculated using similar triangles (see text). The final image \vec{i} results after transformation into image (pixel) coordinates. Lens distortion effects are not considered in the illustration.

Regarding point 3, the mathematical description of the imaging process, the present paper uses the pinhole camera model, with additional correction terms for lens distortion effects. The model (see Fig. 2) is well known and widely applied in deflectometric applications and is therefore only described briefly. A detailed derivation can be found in Ref. 22 for the pinhole camera model and in Ref. 24 for the lens distortion model.

Let $\vec{x}_c = (x_c, y_c, z_c)^T \in R^3$ be a point with coordinates represented in the camera coordinate system. The origin of the camera coordinate system defines the location of the pinhole, or camera center. The camera z -axis coincides with the camera's optical axis (see Fig. 2). Using similar triangles, the projection of \vec{x}_c into the image plane is given by

$$\vec{x}_{ip} = \left(fl \frac{x_c}{z_c}, fl \frac{y_c}{z_c}, fl \right)^T = fl \cdot (x_{ip}, y_{ip}, 1)^T; \quad (1)$$

x_{ip} and y_{ip} are called normalized coordinates. Lens distortion is applied by

$$\begin{pmatrix} x'_{ip} \\ y'_{ip} \end{pmatrix} = \begin{pmatrix} x_{ip} \\ y_{ip} \end{pmatrix} + \begin{pmatrix} x_{ip} (k_1 r^2 + k_2 r^4) \\ y_{ip} (k_1 r^2 + k_2 r^4) \end{pmatrix} + \begin{pmatrix} 2p_1 x_{ip} y_{ip} + p_2 (r^2 + 2x_{ip}^2) \\ 2p_2 x_{ip} y_{ip} + p_1 (r^2 + 2y_{ip}^2) \end{pmatrix} \quad (2)$$

with

$$r^2 = x_{ip}^2 + y_{ip}^2. \quad (3)$$

The first additive correction term, with coefficients k_1 and k_2 , models radial lens distortion effects, the second correction term, with coefficients p_1 and p_2 , models tangential lens distortion effects. The transformation to image pixel coordinates $\vec{i} \in R^2$ is described by

$$\vec{i} = (x_i, y_i)^T = \begin{pmatrix} fl_x & 0 & pp_x \\ 0 & fl_y & pp_y \end{pmatrix} (x'_{ip}, y'_{ip}, 1)^T = K \cdot (x'_{ip}, y'_{ip}, 1)^T, \quad (4)$$

where K is called the intrinsics matrix. It contains the focal length coefficients fl_x and fl_y , i.e. the focal length fl , specified in terms of (direction-dependent) image pixel units, and the principal point coordinates pp_x and pp_y , also specified in image pixel units. Obviously, the image projection is not entirely invertible, as the distance information is lost. However, the point \vec{x}_{ip} on the image plane can be computed from \vec{i} by inverting the calculations in between (the inverse lens distortion function is approximated iteratively). Note that the vector \vec{x}_{ip} is the view ray corresponding to the image pixel \vec{i} because it points from the coordinate origin, i.e. the pinhole, to the respective point on the image plane. Given T_{sc}^{-1} , the view rays are readily transformed to the screen coordinate system.

In summary, the setup is described by a total of 14 parameters per camera,

- six external camera parameters ($o_x, o_y, o_z, \alpha, \beta, \gamma$) and
- eight internal camera parameters ($fl_x, fl_y, pp_x, pp_y, k_1, k_2, p_1, p_2$),

that must be determined by both of the calibration procedures that are detailed in the following section. Throughout the remainder of the present paper, let

$$P : R^3 \mapsto R^2, \vec{i} = P(\vec{x}; T, K, k_1, k_2, p_1, p_2) \quad (5)$$

denote the projection function for the camera as detailed above, with a coordinate transformation matrix T that transforms the point \vec{x} from its respective reference coordinate system into the camera coordinate system, the intrinsics matrix K , and the lens distortion coefficients k_1, k_2, p_1 and p_2 .

3. CALIBRATION PROCEDURES

Although neither of the two calibration procedures in the following sections presents a novel calibration principle, details may differ from other implementations. For this reason, and in order to provide a rather complete description of the entire experimental procedure, both methods are described in detail in the following.

3.1 Stepwise Calibration

The stepwise calibration approach follows the principle of calibrating each part of the system independent from the other components, or consecutively, building on previous partial calibration results where necessary. The stepwise calibration described in the following is a two-step procedure, with the internal camera calibration being the first and the external, geometric calibration of the entire setup being the second step.⁸

For the internal camera calibration, we use the MATLAB Computer Vision Toolbox (The MathWorks, Inc., Natick, MA, USA), which implements the popular technique first published by Zhang.²⁵ The process is repeated for each camera independently. It requires a set of images of a specific calibration pattern, which is a checkerboard pattern (with additional elements to break symmetry), with known grid size. For the set of images, the pattern is repeatedly recorded in varying positions; the poses do not need to be known to the algorithm, but are rather determined during the calculations. In order to define a repeatable process, we specified a series of 29 pattern poses guided by several criteria. The primary objective was to move the pattern across the entire field of view of the camera to identify lens distortion effects reliably. Further design objectives were to record the pattern under a wide range of angles and with the pattern rotated by multiples of 90°. The calibration process starts with extracting the checkerboard grid corners from all images, using them as world points with known 3D coordinates by designating the pattern plane as the x - y -plane, a marked corner point as the world space origin and letting the grid lines define the x - and y -coordinate axis. Let s and m be indices to specify the grid corner points (samples) and the pattern poses (measurements), respectively, $\vec{i}_{s,m} \in R^2$ the extracted image coordinates of the grid corner points, and $\vec{x}_s \in R^3$ their known coordinates in the x - y -plane. (As a side note, this description assumes the pattern to be fixed in the world coordinate system and the camera to be moving. This will become irrelevant, as we will only use the internal camera parameters and discard the externals.) Given the correspondences between $\vec{i}_{s,m}$ and \vec{x}_s , we are searching for a set of parameters that fits the data. This is an optimization problem, which is solved iteratively using the Levenberg-Marquardt algorithm^{26–28} and the total squared reprojection error

$$e_{total} = \sum_{s,m} \left\| P_m(\vec{x}_s) - \vec{i}_{s,m} \right\|_2^2 \quad (6)$$

as error measure, where P_m is the camera projection function according to Eq. (5) for the m -th measurement.²⁵ Note that the intrinsic camera parameters are constrained to be the same for all P_m . The initial parameter estimation required for the non-linear optimization algorithm can be computed directly as the solution of a system of linear equations that is derived from the correspondences between $\vec{i}_{s,m}$ and \vec{x}_s ; the details can be found in Ref. 25.

The camera calibration step yields the internal camera parameters for all cameras. The calculated externals, i.e. relations between the pattern poses and camera positions, are ignored, as there is no obvious way to relate

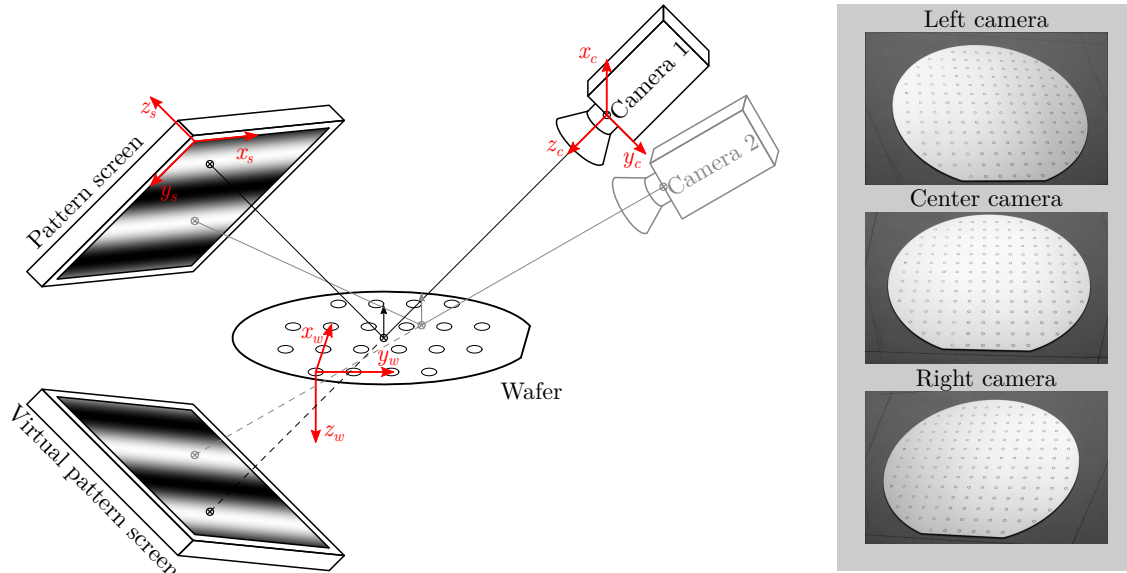


Figure 3. Schematic illustration of the geometric calibration part of the stepwise calibration approach. The regular, orthogonal grid of circle marks is used as a calibration pattern with known mark coordinates to determine the wafer-to-camera coordinate transformations $T_{w,c}$ for all cameras (right). A deflectometric measurement of the wafer yields a correspondence map between camera image pixels (for all involved cameras) and screen points. Using the previously computed camera projection functions, and by introducing the screen mirrored about the wafer plane as a virtual screen, the screen-to-world coordinate transformation T_{sw} is then iteratively optimized to best fit the measurement (left).

them to the pattern screen position. Instead, a reflective calibration target is used for the geometric calibration of the measurement setup. To this purpose, a 150 mm diameter silicon wafer has been marked with a known equidistant, orthogonal grid of circles. The wafer is placed onto the base plane of the measurement setup in such a way, that its entire area is inside the field of view of all cameras. Only one wafer position is used. It defines a preliminary reference coordinate system, with one of the circles marking the origin, the orthogonal grid axes as x - and y -axis and the wafer plane normal vector defining the z -axis (see Fig. 3).

The geometric calibration is divided into two partial steps. First, the camera position is determined in the wafer coordinate system. In the second step, the screen position is determined in relation to the camera. Both parts make use of the parameter optimization with the total reprojection error as error measure, as described above. However, the parameters to be optimized are limited to the three rotation and three translation parameters; the internal camera parameters remain constant.

For the first part of the geometric calibration, the circle centers on the wafer surface assume the role of the grid corner points of the camera calibration pattern (see Fig. 3). As above, their coordinates \vec{x}_s are known with respect to the preliminary reference coordinate system defined by the wafer. The corresponding image coordinates \vec{i}_s can be determined by ellipse detection algorithms (as described in Ref. 29, for instance). With this information, we apply the Levenberg-Marquardt algorithm again with the error measure $\sum_s \left\| P(\vec{x}_s) - \vec{i}_s \right\|_2^2$ to find the camera's extrinsic parameters with respect to the wafer coordinate system, i.e. the camera center $\vec{\sigma} = (o'_x, o'_y, o'_z)^T$ and rotation angles α' , β' and γ' that define the coordinate transformation T_{wc} between the wafer and the camera coordinate system. This first part of the geometric calibration is repeated for all cameras independently.

The second part of the geometric calibration is to determine the external screen parameters. More precisely, we want to find the origin coordinates $\vec{\sigma}'' = (o''_x, o''_y, o''_z)^T$ and rotation angles α'' , β'' and γ'' that define the coordinate transformation T_{sw} between the screen and the wafer coordinate system. In contrast to the previous calibration steps, all cameras participate in the optimization procedure at the same time. We first select a

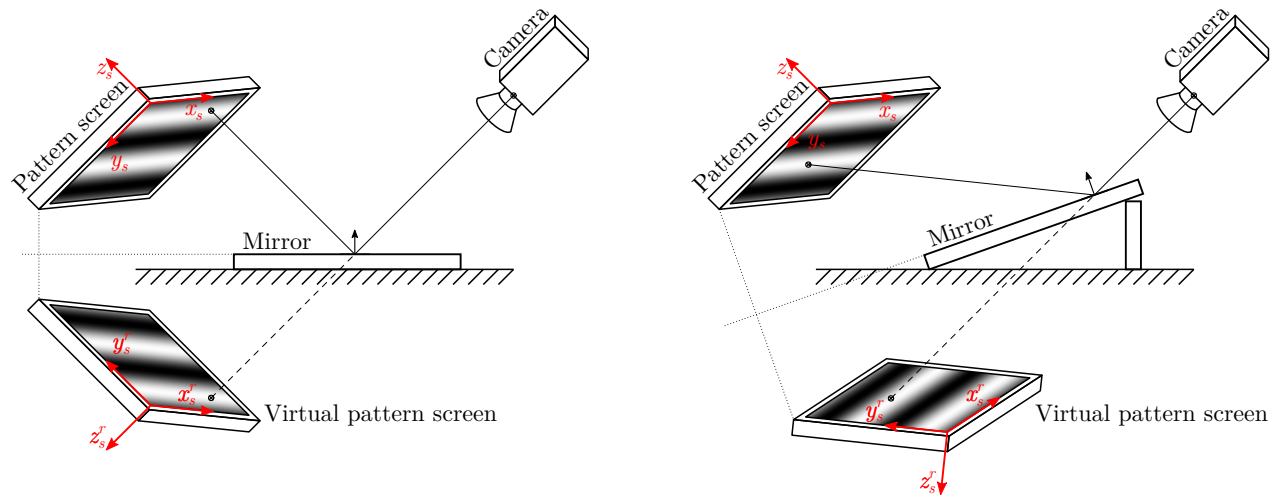


Figure 4. Schematic illustration of the holistic calibration approach. Deflectometric measurements are performed with a planar mirror in different poses (only two are shown). The recorded measurements can be thought of as image data acquired from the virtual screens without the mirror (dashed lines). The virtual screens are identical to the real pattern screen reflected about the mirror planes (dotted lines). The mirror planes do not have to be known a priori; they are also determined by the iterative calibration process.

sample of camera pixels $\vec{i}_{s,c}$ from inside the image area of each camera that shows the reflective wafer surface. The corresponding world points $\vec{x}_{s,c}$ are the points on the pattern screen surface from which the light was originally emitted. Their coordinates, with respect to the screen coordinate system, are known from the phase maps (the z -coordinate is 0 again). We now acknowledge the fact that instead of the light rays being reflected into the cameras at the wafer surface, they could as well originate from a screen mirrored about the wafer surface (see Fig. 3) without changing the acquired camera images. Given an estimate for the external screen parameters, and therefore for T_{sw} , we can transform the points $\vec{x}_{s,c}$ into the wafer coordinate system and then easily calculate the mirrored points $\vec{x}''_{s,c}$ by simply inverting the z -coordinate; remember that the wafer surface defines the x - y -plane of the wafer coordinate system:

$$\vec{x}''_{s,c} = \begin{pmatrix} 1 & 0 & 0 \\ 0 & 1 & 0 \\ 0 & 0 & -1 \end{pmatrix} \cdot (T_{sw}\vec{x}_{s,c}). \quad (7)$$

The Levenberg-Marquardt optimization can be used once more, with the error measure $\sum_{s,c} \left\| P_c(\vec{x}''_{s,c}) - \vec{i}_{s,c} \right\|_2^2$, to find the optimal screen extrinsic parameters mentioned above. Note that the error sum includes all involved cameras now, and that the camera projection functions P_c are entirely known from the external camera calibration step; the parameters to be optimized are only the ones that define the coordinate transformation matrix T_{sw} in Eq. (7).

Finally, to obtain the six external camera parameters as defined in Sec. 2, the screen-to-camera transformation matrix T_{sc} is given by $T_{wc}T_{sw}$. For a detailed description of how to decompose T_{sc} into the external camera parameters, we refer to Ref. 22.

3.2 Holistic Calibration

The idea behind the holistic calibration^{12–14} is taking a number of deflectometric measurements of a planar front surface mirror in different (a priori unknown) poses (see Fig. 4). The correspondence map of each measurement defines correspondences between the image pixels and points in the world with known 3D coordinates in the screen coordinate system that is going to be used as the reference coordinate system (all points in the screen plane have a z -coordinate of 0). Instead of resulting from the real setup with the mirror, the recorded image data

can also be modeled as images of virtual pattern screens (with an inverted screen coordinate system), located at positions that are defined by the real screen position reflected about the respective mirror planes (see Fig. 4). The set of (external and internal) camera parameters and mirror planes that best describe the measurement data can be determined using an iterative optimization technique.

Since the mirror poses need not be known a priori, they also do not have to be precisely defined or accurately positioned. It is useful, however, to specify a few criteria that they should fulfill. They certainly should differ from each other significantly, as repeated measurements using the same pose may reduce noise-related effects but do not generate new information. Particularly, the set union of screen points included in the correspondence maps of all measurements should cover the majority of the extent of the pattern screen. Finally, the minimum number of poses required in practice for a robust optimization has been mentioned to be around five.¹² Led by these criteria, we specify a calibration procedure that includes 16 different mirror poses. The mirror is always positioned to fill as much of the field of view of all three cameras as possible; for most of the poses this is the entire field of view. The first pose is the mirror lying flat on the floor of the setup; the mirror plane resulting from this measurement will later define the base plane of the measurement area. Afterwards, sets of five measurements each are performed with support blocks of three different heights. They are used to generate sloped mirror poses by lifting up, in turn, the left, right, near and far side of the mirror, and finally to elevate the entire mirror by the respective amount. Between measurements, the mirror is repositioned manually.

The unknown variables of the setup include, as described above, the 14 camera parameters for each included camera as well as the mirror planes, each described by their unit normal vector $\vec{n} = (n_x, n_y, n_z)^T$ and distance d from the screen origin. Note that each normal vector is entirely defined by only two components because of the unit length constraint; the remaining component, w.l.o.g n_z , is then determined as $n_z = \sqrt{1 - n_x^2 - n_y^2}$. The number of unknowns is therefore three per mirror pose.

Similar to Sec. 3.1, given the correspondences between image pixels and 3D world coordinates of points on the screen, as described above, we are searching for a set of parameters that fits the data. For feasibility reasons, the Levenberg-Marquardt optimization is performed on a subset of all pixel-screen coordinate correspondences: we sample the camera image pixels using a regular, square grid with a horizontal and vertical sample distance of 50 pixels. The required initial parameter estimation is based on manual measurements of the geometric setup, and on the data sheet of the used cameras and objectives. The total squared reprojection error is used as error measure, which is calculated similar to the last step in the stepwise calibration.

Let $\vec{x}_{s,c,m} \in R^3$ and $\vec{i}_{s,c,m} \in R^2$ be the s -th sample of corresponding screen point and image pixel, respectively, of the c -th camera from the m -th measurement (i.e. mirror pose). Further, let \vec{n}_m and d_m be the estimation of the unit normal vector and distance from the origin, respectively, of the mirror plane in the m -th measurement during a given iteration of the optimization process. Finally, let P_c denote the estimation of the projection function for the c -th camera according to Eq. (5) during the same iteration. For the sake of readability, we omit iteration indices and the parameters of P_c . The reflection of a point $\vec{x} \in R^3$ about a plane with normal vector \vec{n} and distance d onto \vec{x}^r is given by

$$\vec{x}_{s,c,m}^r = (I - 2\vec{n}\vec{n}^T) \vec{x}_{s,c,m} + 2d\vec{n}, \quad (8)$$

where I is the identity matrix; the 3×3 -matrix $I - 2\vec{n}\vec{n}^T$ is called a Householder matrix.²² Using these notations, the total squared reprojection error that is minimized by the optimization algorithm is

$$e_{total} = \sum_{s,c,m} \left\| P_c(\vec{x}_{s,c,m}^r) - \vec{i}_{s,c,m} \right\|_2^2. \quad (9)$$

4. EXPERIMENTS AND ANALYSES

The basic framework of the deflectometry measuring station (see Fig. 5) is made of strut profiles ($80 \times 80 \text{ mm}^2$). For flexible positioning, the pattern screen and the cameras can be mounted on adaptable traverses within the basic framework of $680 \times 400 \times 650 \text{ mm}^3$. For the present experimental study, a 32-inch monitor (AOC U3277PQU) with an IPS panel is used to display the patterns. The monochrome USB-3 cameras (Basler acA1920-40um) have a resolution of 2.3 MP and the objectives used (Lensation C8M2514GSV2) have a fixed focal length of 25 mm.

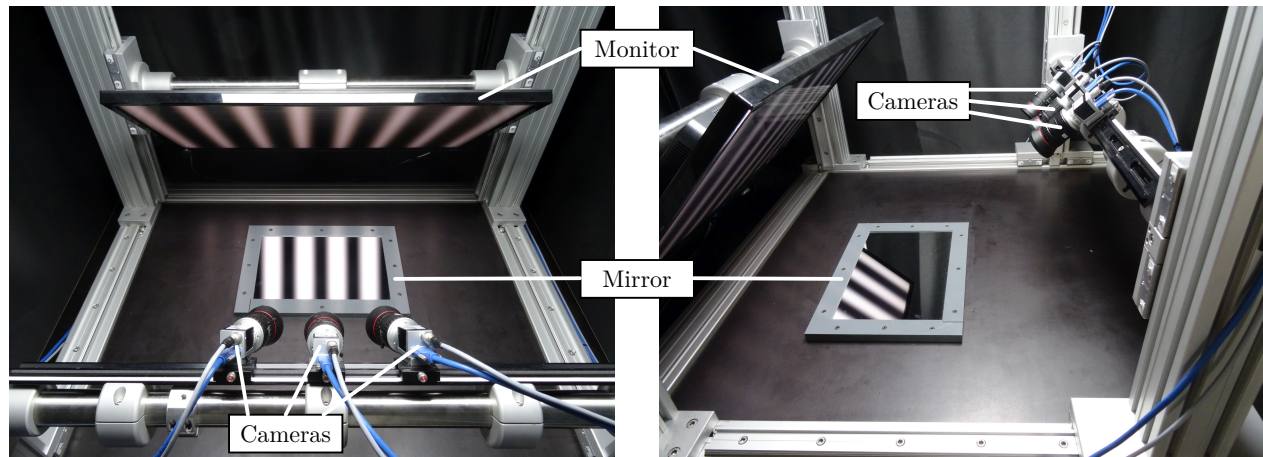


Figure 5. Front view (left) and side view (right) photograph of the deflectometric measurement station used for the experiments. The mirror in the images is the calibration mirror used for holistic calibration, arranged in its first pose, lying flat on the floor of the setup (see Sec. 3.2).

In order to assess the reproducibility of the two calibration approaches experimentally, we repeat the procedures described in Sec. 3 ten times each and evaluate the variability of the resulting internal and external parameters (experiment E1). Assuming that the measurement setup itself does not change in between the repeated calibrations, the measured parameter variability is attributable to two sources: physical measurement noise and geometric variations in the (manual) placement of the calibration pattern or mirror.

In order to separate these two effects, we repeat both procedures again, this time performing all image acquisition and measurement processes related to a calibration mirror or pattern position ten times in a row before rearranging the mirror or pattern (experiment E2). The resulting parameter variability therefore must be attributed entirely to measurement noise.

Finally, in order to interpret the effects of parameter variability on the measurement process, we calculate the variability of image coordinates of a set of world points projected onto the image planes of the calibrated cameras.

For all examinations, a Gaussian distribution of the parameter measurements is assumed and the standard deviation of the examined variables is used as a measure of their variability. The comparative assessment of two single parameter variabilities (e.g. variability of rotation angle α from holistic calibration in experiment E1 versus experiment E2) is described straightforward by their ratio. For more general comparative statements on the variability of parameter groups (e.g. external parameters), the ratios of the considered parameters are averaged using the geometric mean. The geometric mean is chosen as averaging function instead of the common mean because of symmetry considerations concerning the reciprocal ratios. One would expect the average of the reciprocal ratios and the reciprocal of the average of the ratios to be equal. The geometric mean satisfies this, the common mean does not (as can easily be seen using the ratios 2 and 0.5, for instance).

5. RESULTS

Table 1 lists the standard deviations for all parameters, calculated after ten repeated calibrations, for experiments E1 and E2 and for both the holistic and stepwise calibration procedure. Unsurprisingly, the data almost consistently reveal the variability in experiment E1 to be higher than in experiment E2. The only exception is the first radial lens distortion coefficient k_1 from holistic calibration, for which a standard deviation of 0.0006 is determined in E1 whereas it is 0.0010 in E2.

The average ratio of parameter variabilities between experiment E1 and E2, aggregated over all parameters, is 2.16 for the holistic calibration but 4.65 for the stepwise approach (see Tab. 2). Measurement noise therefore

Table 1. Parameter variability (standard deviation from ten repeated calibrations), aggregated over three cameras

	Stepwise Experiment E1	Holistic Experiment E1	Stepwise Experiment E2	Holistic Experiment E2
o_x [mm]	0.14	0.13	0.04	0.03
o_y [mm]	0.26	0.84	0.07	0.44
o_z [mm]	0.10	1.19	0.02	0.48
α [°]	0.039	0.074	0.009	0.038
β [°]	0.021	0.017	0.005	0.008
γ [°]	0.018	0.006	0.003	0.004
fl_x [px]	2.7	3.1	0.7	1.5
fl_y [px]	2.3	3.1	0.6	1.5
pp_x [px]	1.6	1.3	0.2	0.6
pp_y [px]	3.5	1.0	0.8	0.2
k_1 []	0.0023	0.0006	0.0004	0.0010
k_2 []	0.0552	0.0066	0.0081	0.0033
p_1 []	0.000 209	0.000 029	0.000 049	0.000 015
p_2 []	0.000 061	0.000 137	0.000 011	0.000 039
Image coordinates [px]	0.89	0.78	0.16	0.26

Table 2. Average parameter variability ratio between experiment E1 and experiment E2, aggregated over three cameras and parameter groups (a ratio value > 1 means larger parameter variability in E1 than in E2 and vice versa); average calculated by geometric mean (see Sec. 4)

	Holistic	Stepwise	Both
External parameters	2.20	4.27	3.06
Internal parameters	2.12	4.95	3.24
All parameters	2.16	4.65	3.16

Table 3. Average parameter variability ratio between holistic and stepwise calibration, aggregated over three cameras and parameter groups (a ratio value > 1 means larger parameter variability in stepwise than in holistic calibration and vice versa); average calculated by geometric mean (see Sec. 4)

	Experiment E1	Experiment E2	Both experiments
External parameters	1.62	3.15	2.26
Internal parameters	0.50	1.16	0.76
All parameters	0.83	1.78	1.21

accounts for 32% of the parameter variability for the holistic calibration, but only for 18% when using the stepwise approach.

The parameter variability comparison between the calibration approaches does not behave uniformly (see Tab. 3). Whereas the measured variability of the internal parameters is only half as high for holistic as for stepwise calibration in experiment E1 (average ratio: 0.50) and on comparable levels in experiment E2 (average ratio: 1.16), the external parameters reveal a completely different behavior. The external parameter variability turns out to be higher, in both experiments, for the holistic compared to stepwise calibration, by an average factor of 2.26.

The image coordinate variability is comparable for both calibration approaches, with an average of 0.84 and 0.21 camera pixels for E1 and E2, respectively (see Tab. 1).

6. DISCUSSION

As with all real-world measurement processes, the calibration procedures described in Sec. 3 unavoidably possess some amount of uncertainty regarding the calibration results. Different effects can contribute to this, for instance physical measurement noise, changing environmental conditions between measurements or systematic bias effects inherent to the measurement procedure. Two concepts are commonly used to describe, compare and/or quantify the reliability of a measurement process: on the one hand, the accuracy describes how close the average measurement result is to the (usually unknown) real value that is measured; the accuracy especially encompasses systematic biases of the measurement procedure. The precision, on the other hand, describes how much measurement results vary if repeated under the same conditions. The reproducibility experiments in the present paper examine the precision of the stepwise and holistic calibration procedures, whereas previous comparative assessments based on subsequent surface measurements¹² are more focused on their accuracy.

The experiment E2 is designed to reveal the variability of the calibrated parameters purely resulting from physical measurement noise, whereas the repetition of the entire procedures in experiment E1 also contains manual interactions as an additional source of variability. The higher variability values in E1 than in E2 for almost all parameters are therefore expectable. The one exception, the first radial lens distortion coefficient k_1 from holistic calibration (see Tab. 1), is surprising. Regarding that the calibrated values of k_1 are in the order of -0.23 , for all three cameras, the measured variabilities of 0.0006 in E1 and 0.0010 in E2 are well below 0.5% in both experiments. For an increasing number of repetitions, we would expect the variabilities for both experiments to converge to a similar value. It must also be taken into account that radial lens distortion is described by the interaction of k_1 and k_2 (see Eq. (2)). When aggregating over both coefficients, the average variability ratio between experiment E1 and E2 (using the geometric mean) for holistic calibration is 1.11, which supports the assumption that the radial lens distortion calibration is dominated by noise effects rather than other influences.

Regarding the inter-experiment variability ratios (i.e. the variability of a parameter in E1 divided by its variability in E2), it is interesting to find lower ratio values, for most parameters, for the holistic calibration than for the stepwise approach. In fact, aggregated over all parameters, the average inter-experiment variability ratio of 2.16 for holistic calibration is significantly lower than 4.65 for stepwise calibration; the numbers are similar when aggregating over the internal parameters or over the external parameters only (see Tab. 2). As experiment E2 determines the purely noise-related parameter variability, the excess portion of the variability measured in

experiment E1 (i.e. the portion of the inter-experiment variability ratio above 1) may be interpreted as a measure of the robustness of the calibration procedure against the operator-dependent handling of the calibration pattern or mirror. The numbers above therefore suggest that the holistic calibration has significantly better robustness against such operator-dependent effects than the stepwise approach.

On the other hand, the experimental results also reveal that the holistic calibration procedure is more susceptible to measurement noise than the stepwise one, as evidenced by column E2 in Tab. 3. Regarding the internal camera parameters, the average variability is similar for both approaches, yet a little higher, by a factor of 1.16, after holistic calibration. For the external parameters, however, the average ratio increases to 3.15. With respect to effective precision measured in experiment E1, the higher noise-susceptibility of the holistic approach is somewhat mitigated by its higher robustness to other sources of parameter variability. Nevertheless, the external parameters in particular still exhibit a higher average variability in E1 for the holistic than for the stepwise calibration, by an average factor of 1.62 (see Tab. 3).

This latter result regarding the precision of the two compared calibration techniques is unexpected and gains particular importance in view of the fact that the holistic approach has been shown to be more accurate than the stepwise approach, with regard to their respective application to surface measurements.¹²

While the results are interesting in and of themselves, we do not have a conclusive explanation for them yet. Possible approaches to explain the measured differences in precision include the non-validity of inherent assumptions. For instance, both calibration techniques assume that the calibration wafer or the calibration mirror are essentially planar. We know from high-precision point-wise distance measurements that this assumption is violated, to different degrees, for both reflective surfaces. Furthermore, the pattern screen is also modeled as a plane, although the monitor surface exhibits a clearly visible convex curvature (caused by its fixation at an angle of approximately 45° with relation to the horizontal plane).^{30,31} The monitor curvature is, of course, present for both calibration techniques. However, it may have a stronger influence on the holistic calibration because the measurements performed with varying mirror poses cover a large proportion of the monitor area, whereas the single wafer pose in the stepwise calibration reflects the light from only a smaller, central area of the screen into the cameras. Other, more subtle effects may add to that as the camera view rays hit the monitor under smaller angles in the periphery than at its center due to the geometry of the setup. These include the refraction of the light rays at the front surface of the monitor,¹² as well as a deviation between the intersection point of a view ray with the screen and the center of the captured elliptical blur spot on the screen.¹² Finally, mechanical vibrations may also play a minor role, particularly because different exposure times were used for the calibration pattern, the marked wafer, and the calibration mirror, due to different lighting conditions or reflectivity.

Further research should look into simulations of the deflectometric setup and the measurement and calibration procedures in order to examine these hypotheses and grade their effects. The simulation results can then provide the basis for further developments to model and incorporate the relevant missing aspects into the measurement model and the calibration procedure.

ACKNOWLEDGMENTS

This work was funded by the programme Science and Technology of Nanosystems in the Research Field Key Technologies of the Helmholtz Association.

REFERENCES

- [1] Chang, J. S., Facchetti, A. F., and Reuss, R., “A circuits and systems perspective of organic/printed electronics: review, challenges, and contemporary and emerging design approaches,” *IEEE J. Emerg. Sel. Top. Circuits Syst.* **7**, 7–26 (2017).
- [2] Schwartz, D. E., Rivnay, J., Whiting, G. L., Mei, P., Zhang, Y., Krusor, B., Kor, S., Daniel, G., Ready, S. E., Veres, J., and Street, R. A., “Flexible hybrid electronic circuits and systems,” *IEEE J. Emerg. Sel. Top. Circuits Syst.* **7**, 27–37 (2017).
- [3] Saengchairat, N., Tran, T., and Chua, C.-K., “A review: additive manufacturing for active electronic components,” *Virtual Phys. Prototyp.* **12**, 31–46 (2017).

- [4] Hajisaeid, E., Haghzadeh, M., Shone, M., Mooney, P., Panwar, A., Barry, C., Mead, J., Armiento, C., and Akyurtlu, A., "Printed tunable frequency selective surface on a developed flexible functionalized ceramic-polymer based substrate," in [2016 IEEE International Symposium on Phased Array Systems and Technology (PAST)], 1–5, IEEE (2016).
- [5] Beyerer, J., Puente León, F., and Frese, C., [Machine Vision: Automated Visual Inspection: Theory, Practice and Applications], Springer, Berlin (2016).
- [6] Huang, L., Idir, M., Zuo, C., and Asundi, A., "Review of phase measuring deflectometry," *Opt. Lasers Eng.* **107**, 247–257 (2018).
- [7] Kammel, S. and Puente León, F., "Deflectometric measurement of specular surfaces," *IEEE Trans. Instrum. Meas.* **57**, 763–769 (2008).
- [8] Knauer, M. C., Kaminski, J., and Häusler, G., "Phase Measuring Deflectometry: a new approach to measure specular free-form surfaces," in [Optical Metrology in Production Engineering], Osten, W. and Takeda, M., eds., *Proc. SPIE* **5457**, 366–376, SPIE (2004).
- [9] Knauer, M. C., [Absolute Phasennessende Deflektometrie], Lehrstuhl für Mikrocharakterisierung, Erlangen (2006).
- [10] Tarini, M., Lensch, H. P., Goesele, M., and Seidel, H.-P., "3D acquisition of mirroring objects using striped patterns," *Graph. Models* **67**, 233–259 (2005).
- [11] Zhou, T., Chen, K., Wei, H., and Li, Y., "Improved system calibration for specular surface measurement by using reflections from a plane mirror," *Appl. Opt.* **55**, 7018–7028 (2016).
- [12] Faber, C., [New Methods and Advances in Deflectometry], Erlangen Scientific Press, Erlangen (2012).
- [13] Ren, H., Gao, F., and Jiang, X., "Iterative optimization calibration method for stereo deflectometry," *Opt. Express* **23**, 22060–22068 (2015).
- [14] Xu, Y., Gao, F., Zhang, Z., and Jiang, X., "A holistic calibration method with iterative distortion compensation for stereo deflectometry," *Opt. Lasers Eng.* **106**, 111–118 (2018).
- [15] Ren, H., Jiang, X., Gao, F., and Zhang, Z., "Absolute height measurement of specular surfaces with modified active fringe reflection photogrammetry," in [Interferometry XVII: Advanced Applications], Furlong, C., Gorecki, C., de Groot, P. J., and Novak, E. L., eds., *Proc. SPIE* **9204**, 920408, SPIE (2014).
- [16] Liu, Y., Huang, S., Zhang, Z., Gao, N., Gao, F., and Jiang, X., "Full-field 3D shape measurement of discontinuous specular objects by direct phase measuring deflectometry," *Sci. Rep.* **7**, 10293 (2017).
- [17] Balzer, J. and Werling, S., "Principles of shape from specular reflection," *Measurement* **43**, 1305–1317 (2010).
- [18] Perard, D. and Beyerer, J., "Three-dimensional measurement of specular free-form surfaces with a structured-lighting reflection technique," in [Three-Dimensional Imaging and Laser-based Systems for Metrology and Inspection III], Harding, K. G. and Svetkoff, D. J., eds., *Proc. SPIE* **3204**, 74–80, SPIE (1997).
- [19] Balzer, J., Werling, S., and Beyerer, J., "Regularization of the deflectometry problem using shading data," in [Two- and Three-Dimensional Methods for Inspection and Metrology IV], Huang, P. S., ed., *Proc. SPIE* **6382**, 63820B, SPIE (2006).
- [20] Pak, A., "Stability of absolute depth reconstruction from deflectometric measurement data," in [Interferometry XVII: Techniques and Analysis], Creath, K., Burke, J., and Schmit, J., eds., *Proc. SPIE* **9203**, 92030E, SPIE (2014).
- [21] Liu, M., Hartley, R., and Salzmann, M., "Mirror surface reconstruction from a single image," *IEEE Trans. Pattern Anal. Mach. Intell.* **37**, 760–773 (2015).
- [22] Hartley, R. and Zisserman, A., [Multiple View Geometry in Computer Vision], Cambridge University Press, Cambridge, second ed. (2006).
- [23] Vince, J., [Mathematics for Computer Graphics], Springer, London, fifth ed. (2017).
- [24] Drap, P. and Lefèvre, J., "An exact formula for calculating inverse radial lens distortions," *Sensors* **16** (2016).
- [25] Zhang, Z., "A flexible new technique for camera calibration," *IEEE Trans. Pattern Anal. Mach. Intell.* **22**, 1330–1334 (2000).

- [26] Levenberg, K., "A method for the solution of certain non-linear problems in least squares," *Quart. Appl. Math.* **2**, 164–168 (1944).
- [27] Marquardt, D. W., "An algorithm for least-squares estimation of nonlinear parameters," *J. Soc. Indust. Appl. Math.* **11**, 431–441 (1963).
- [28] Moré, J. J., "The Levenberg-Marquardt algorithm: implementation and theory," in [*Numerical Analysis*], Watson, G. A., ed., *Lecture Notes in Mathematics* **630**, 105–116, Springer, Berlin, Heidelberg (1978).
- [29] Davies, E. R., [*Computer and Machine Vision: Theory, Algorithms, Practicalities*], Academic Press, Waltham, MA, fourth ed. (2012).
- [30] Petz, M., [*Rasterreflexions-Photogrammetrie: Ein neues Verfahren zur geometrischen Messung spiegelnder Oberflächen*], Shaker, Aachen (2006).
- [31] Bartsch, J., Kalms, M., and Bergmann, R. B., "Improving the calibration of phase measuring deflectometry by a polynomial representation of the display shape," *J. Eur. Opt. Soc. Rapid Publ.* **15** (2019).